Supplement of Weather Clim. Dynam., 5, 109–132, 2024
https://doi.org/10.5194/wcd-5-109-2024-supplement

Supplement of

European summer weather linked to North Atlantic freshwater anomalies in preceding years

Marilena Oltmanns et al.

Correspondence to: Marilena Oltmanns (marilena.oltmanns@noc.ac.uk)

This supplement is split into two parts. Part 1 includes the mass balances associated with the three freshwater indices, the composites of the winters preceding the ten hottest minus the ten coldest summers, and an example of the mass balance revealed through in-situ hydrographic observations. Part 2 includes significance analyses to test the robustness of the freshwater indices against excluding double events, alterations of the subsampling technique, and pre-filtering of the involved time series.

S1 Mass balance analyses

The following sections include the evaluation of the mass balances obtained from the freshwater indices F_E, F_W and ΔSST (S1.1), the surface mass balance obtained from the SST composite (S1.2), and a demonstration of the mass balance with hydrographic observations (S1.3).

S1.1 Surface mass balance for freshwater indices

Taking advantage of the strong relationships between the NAO_S subsets (F_E and F_W) and the subsequent SST anomalies, we regress each term of Eq. (5) in the manuscript onto the indices and evaluate the surface mass balance over the subpolar cold anomaly regions within the 95% confidence lines (Figs. S1a and S2a).

Considering that the mean mixed layer deepens from summer to winter, reaching its maximum in late winter, the integrated anomalies in the surface heat and buoyancy fluxes during autumn are predominantly driven by existing anomalies in the density profile. For instance, an anomalously warm and light layer of water will lead to increased ocean heat and buoyancy losses once it has been entrained (Timlin et al., 2002). Thus, given that the anomalies in B_n and E_n are largely compensating for each other when integrated over autumn (the period of rapid mixed layer deepening), we focussed on the winter period (January through to March), when the amplitude and variability of the surface fluxes is largest. However, if we integrate the terms on the righthand side of Eq. (5) over autumn and winter, instead of only winter, the magnitude of the integrated anomalies does not appreciably change and their signs remain the same.

First, we estimate the 'active' component of the mass convergence (A). On the timescales and spatial scales considered, the strongest horizontal velocities result from geostrophic flows such as eddies and the subpolar gyre circulation. These geostrophic flows do not contribute to a net mass increase as they occur along lines of constant density and pressure. The largest ageostrophic surface flow in the open ocean results from the wind forcing, which we evaluate using the wind stresses from the atmospheric reanalysis ERA5. Integrated over the winter period (January through to March), we find that neither the horizontal Ekman transports nor the vertical Ekman pumping can account for the density increase associated with the cold anomaly. They are not significantly correlated with the freshwater indices, their amplitudes are too small, and their directions are inconsistent with the cold anomaly (Figs. S1a, b and S2a, b).

Next, we estimate the surface buoyancy flux anomalies with:

$$B = \frac{g\alpha}{c_p} Q + g\beta S\,(P - E)\,, \tag{S1}$$

where c_p is the heat capacity, Q is the heat flux (positive downward) and $P - E$ is the freshwater flux in kg m^{-2} s^{-1} (Gill, 1982). The thermal and haline expansion coefficients α and β were estimated using Gibbs Seawater Routines (McDougall et al., 2009). Specifically, we used a nominal pressure of 10 db, a salinity of 34.5 g kg^{-1} and the observed skin temperature from ERA5. Likewise, the direct salinity Eq. (S1) was also estimated with 34.5 g kg^{-1}, corresponding to a typical salinity in the subpolar region. However, the results are not sensitive to the exact values.

After evaluating the buoyancy fluxes with 6-hourly ERA5 output and regressing them on the freshwater indices, we find that they do not match the distribution of the SST (Figs. S1c and S2c). The surface heat fluxes, which have the largest contribution to the buoyancy fluxes, are also not significantly correlated with the indices (Figs. S1d and S2d). When averaged over the cold anomaly regions, enclosed by the 95% confidence lines, and integrated over the winter, the buoyancy flux anomaly associated with the F_E subset reflects an anomalous mass decrease of $\sim$7 kg m^{-2} whereas the cold anomaly implies a mass increase of $\sim$204 kg m^{-2}. Likewise, the buoyancy flux anomaly associated with the F_W subset reflects a mass decrease of $\sim$4 kg m^{-2}, whereas the cold anomaly implies a mass increase of $\sim$69 kg m^{-2}. For both subsets, we used a mean density of $\rho_{mean} \approx 1000$ kg m^{-3} to estimate the mass anomaly associated with the cold anomaly.

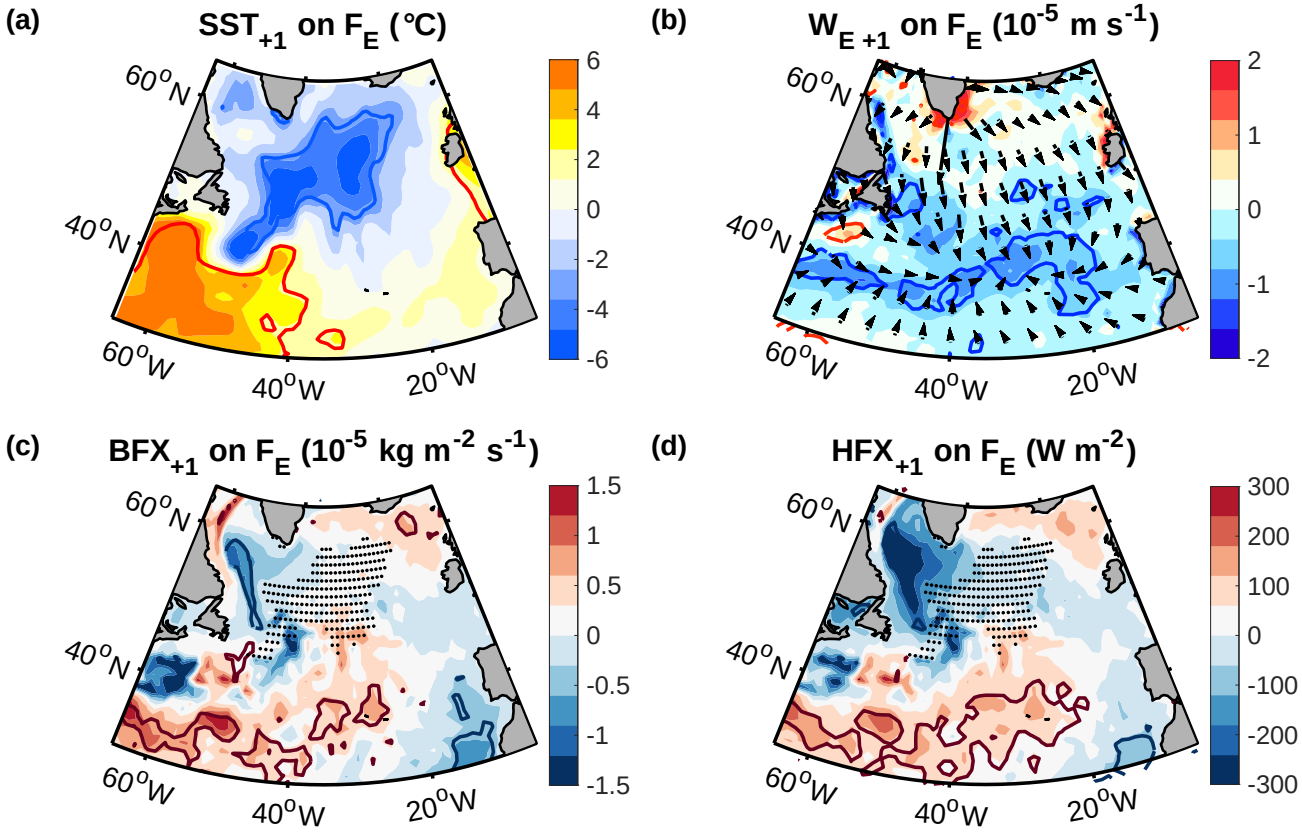

Figure S1. Regression of (a) the SST, (b) the vertical Ekman velocity (positive upward), (c) the buoyancy flux anomaly (positive downward) and (d) the surface heat fluxes (also positive downward) in winter (January through March) on F_E from the preceding summer. The arrows in (b) indicate the direction of the horizontal Ekman transports and the dots in (c) and (d) show the region used for the mass balance calculations, corresponding to the cold anomaly region. Contours encompass regions that are significant at the 95% confidence level.

Since none of the potential, active drivers of density anomalies on the righthand side of Eq. (5) can account for the density increase associated with the cold anomalies, we conclude that the density increase associated with the cold anomalies must be balanced by a density decrease associated with freshwater anomalies. The buoyancy fluxes represent the largest term on the righthand side of Eq. (5), and thus determine the uncertainty of the obtained salinity estimates, amounting to $\sim$4% for the F_E subset and $\sim$6% for the F_W subset.

To verify the robustness of the results, we tested different integration periods and regions for the mass balance calculations. For instance, we also integrated the transports and surface fluxes from September to March instead of January to March, and we extended the investigated region over the full cold anomaly region, over which the SST anomaly is negative. In each case, the results did not change appreciably.

In addition, we repeated the analyses for the un-subsampled ΔSST index (Fig. 7a). In this case, we obtain a mean mixed layer depth of $\sim$250 m in the blue 95% confidence region (Fig. S3), a negative mass anomaly of ~ -1 kg m^{-2} resulting from the surface buoyancy fluxes, and a positive mass anomaly of $\sim +18$ kg m^{-2} associated with the cold SST anomaly. Thus, estimating the sea surface salinity anomaly by assuming density compensation, we obtain a sea surface salinity of ~ -0.10 g kg^{-1}, averaged over the cold anomaly region enclosed by the 95% confidence lines. The overall uncertainty that results from neglecting the terms on the righthand side of Eq. (5) amounts to 6% in the 95% confidence region.

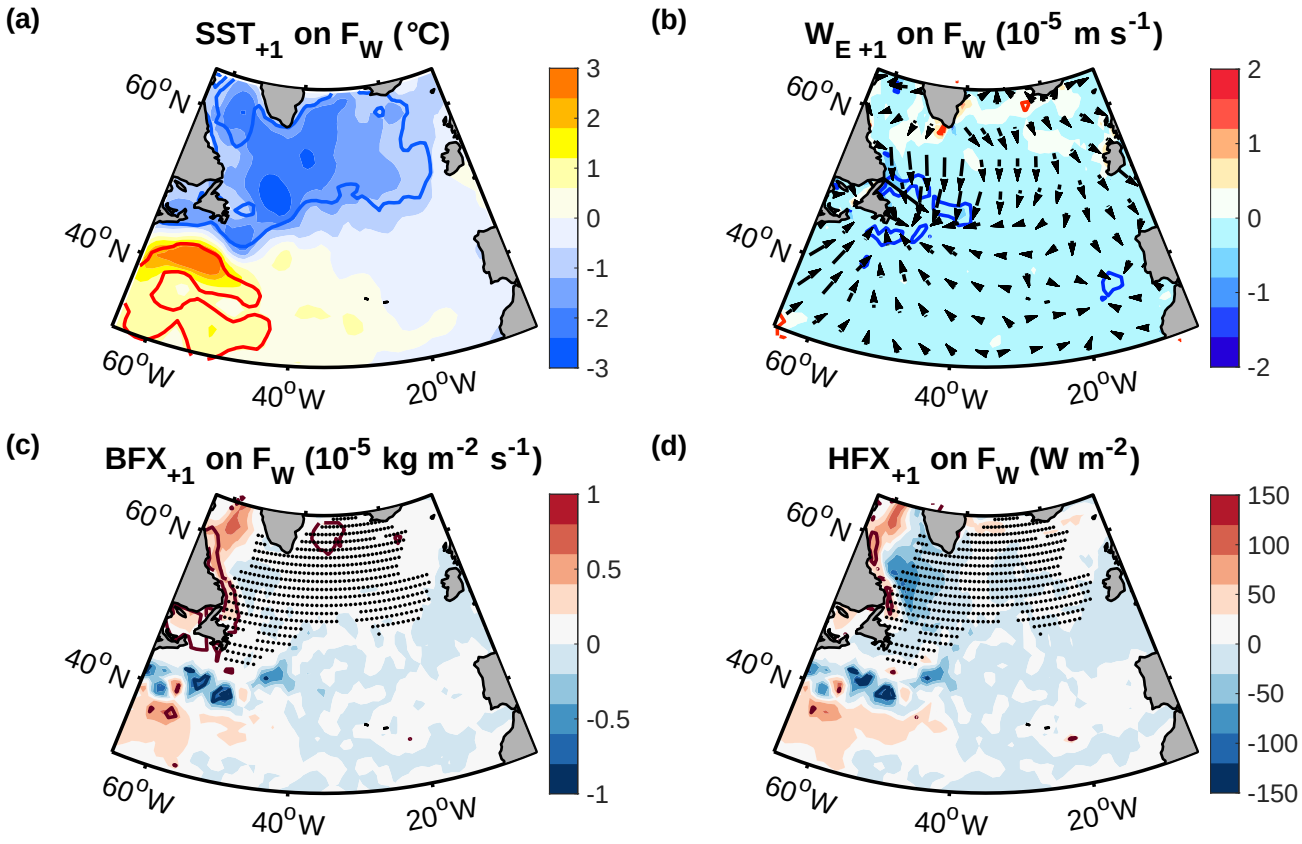

Figure S2. Regression of (a) the SST, (b) the vertical Ekman velocity (positive upward), (c) the buoyancy flux anomaly (positive downward) and (d) the surface heat fluxes (also positive downward) in winter (January through March) on F_W from the preceding summer. The arrows in (b) indicate the direction of the horizontal Ekman transports and the dots in (c) and (d) show the region used for the mass balance calculations. Contours encompass regions that are significant at the 95% confidence level.

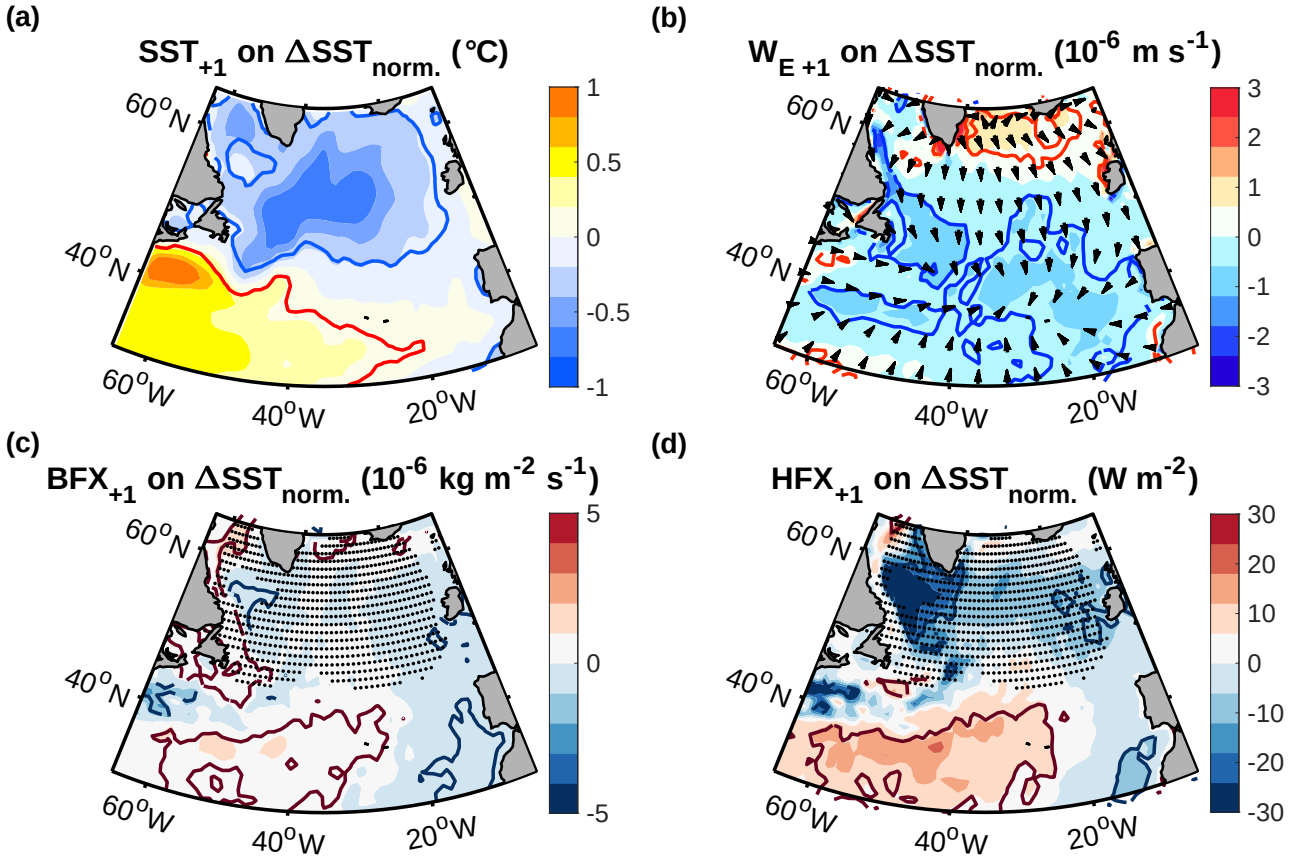

Figure S3. Regression of (a) the SST, (b) the vertical Ekman velocity (positive upward), (c) the buoyancy flux anomaly (positive downward) and (d) the surface heat fluxes (also positive downward) in winter (January through March) on the normalised ΔSST index (Fig. 7a). The arrows in (b) indicate the direction of the horizontal Ekman transports and the dots in (c) and (d) show the region used for the mass balance calculations. Contours encompass regions that are significant at the 95% confidence level.

S1.2 Surface mass balance of the SST composite and trend

We further carried out a mass balance analysis for the composites of the cold anomaly in the winters preceding the 10 warmest relative to the 10 coldest summers over Europe (Fig. 10). Thus, we again evaluated the terms in Eq. (5) over the cold anomaly region and the winter, where now, the subscript n refers to anomalies associated with the composites.

After evaluating each term in the mass balance equation, we obtain similar patterns compared to those associated with the two NAO subsets (Fig. S4). Again, we find that none of the density drivers on the righthand side of Eq. (5) show a significant signal over the cold anomaly region, and their amplitudes cannot account for the density increase implied by the cold anomaly. The mean mixed layer depth in the cold anomaly region (enclosed by the 95% confidence lines) is now $\sim$290 m, the surface buoyancy flux, which is the largest term on the righthand side of Eq. (5), amounts to $\sim +1.2$ g kg^{-1} while the density anomaly implied by the cold anomaly is ~ -44 g kg^{-1}. Thus, the uncertainty of the estimated freshwater anomaly (Fig. 10e) amounts to $\sim$3%.

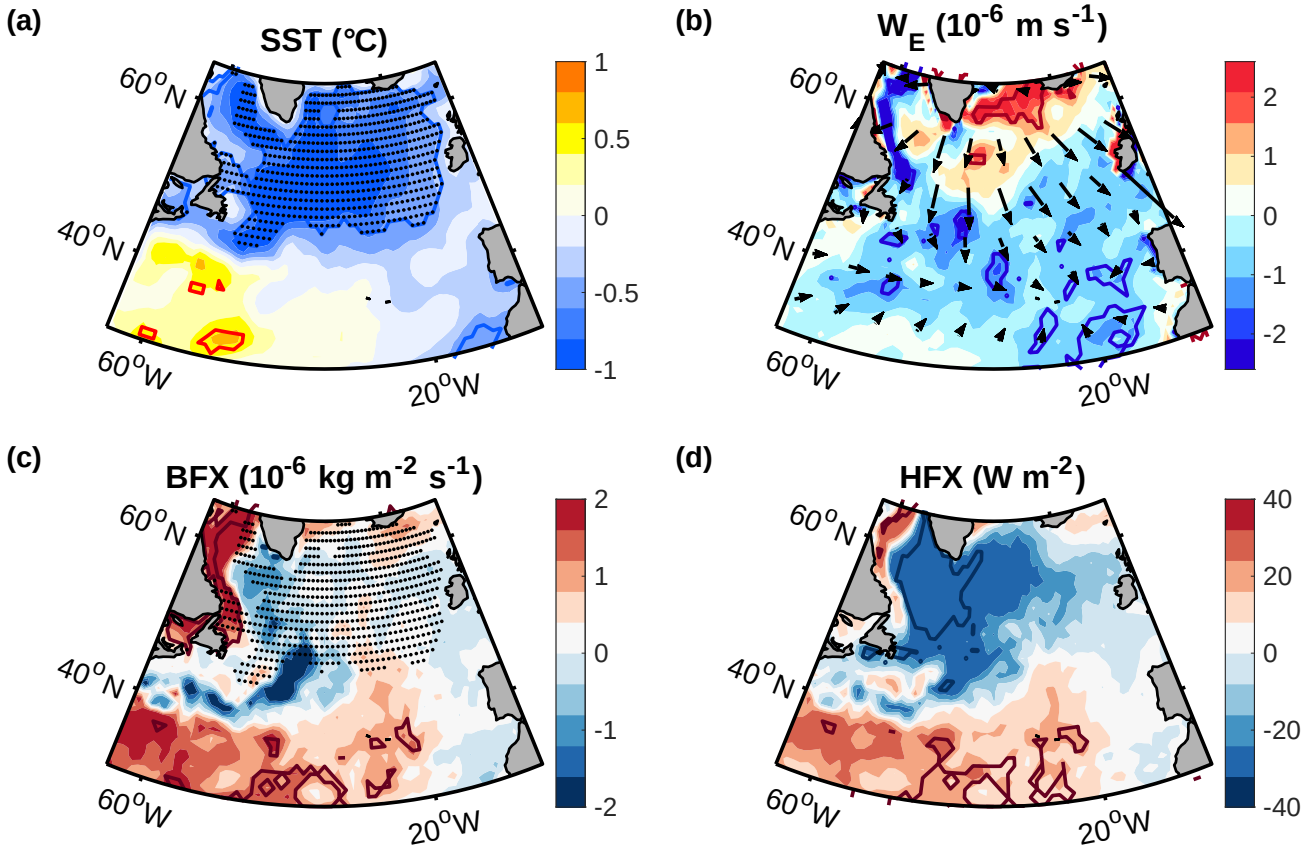

Figure S4. (a,b,c) Anomaly of (a) the SST, (b) the vertical Ekman velocity (positive upward), (c) the buoyancy flux anomaly (positive downward), and (d) the surface heat flux (also positive downward) in the 10 winters (January through March) before the warmest summers minus the 10 winters before the 10 coldest summers (Fig. 10). The arrows in (b) indicate the direction of the horizontal Ekman transports and the dots in (a) and (c) mark the region of the mass balance calculations.

S1.3 Comparison with in-situ observations

To demonstrate the density compensation between temperature and salinity anomalies, we use mixed layer profiles from Argo floats in the subpolar region (Holte et al., 2017). We focus on the extreme winters 2015 and 2016, which were characterised by particularly large surface fluxes and deep convection (Yashayaev and Loder, 2017; Piron et al., 2017).

In both winters, the temperature and salinity anomalies are well-correlated with each other ($r \approx 0.72$, $p \approx 5 \cdot 10^{-242}$, based on 1532 profiles). Moreover, the observed salinity anomalies are well-aligned with the estimated salinity anomalies, obtained by assuming density compensation (Fig. S5). The root mean square error associated with the mass balance estimate amounts to $\sim$0.09 g kg^{-1}, which is smaller than that of currently available salinity products (Bao et al., 2019; Xie et al., 2019).

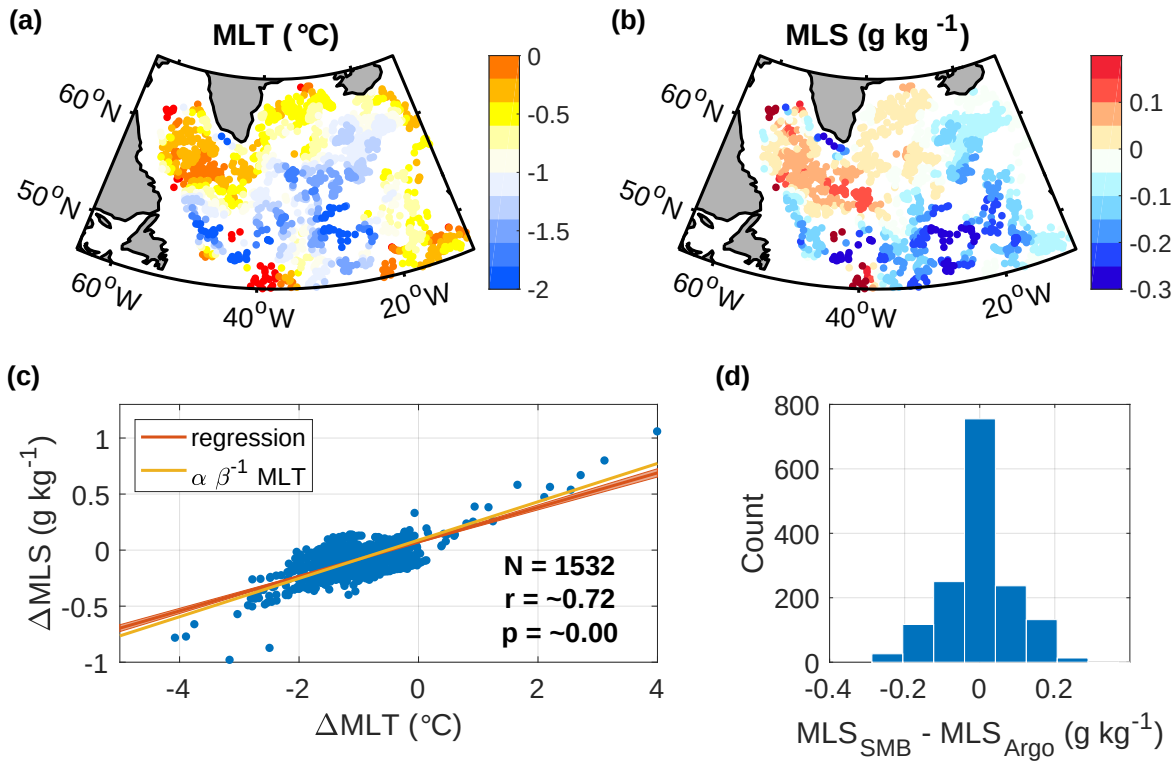

Figure S5. (a,b) Mixed layer temperature (MLT) and salinity (MLS) anomalies in the winters of 2015 and 2016 (January to April), derived from Argo profiles (Holte et al., 2017). The anomalies are relative to the climatological mean, estimated by averaging all other wintertime profiles within 2° longitude and 1° latitude. (c) Linear regression of the observed MLS anomalies on the MLT anomalies (red line), and the MLS estimate obtained by assuming density compensation (yellow line). (d) Differences between the estimated and observed MLS anomalies. The associated root mean square error is $\sim$0.09 g kg^{-1}.

S2 Robustness and significance tests

In this section, we conduct sensitivity tests to assess the robustness of the freshwater indices F_E, F_W, and ΔSST. Considering the different weaknesses of each index, the analyses for each index are different. F_E only includes a low number of years. Thus, we test the sensitivity of the results to including and excluding individual years. For F_W, the sample size is larger, such that adding or removing individual years has almost no effect on the results. Thus, we test the sensitivity of the results to the number of years included in increments of 5 years. Finally, the ΔSST index is characterised by high autocorrelations. Thus, we test if the results remain significant if we lowpass filter European summer weather and assume a lower number of degrees of freedom.

We start with the F_E subset. If we include the outlier in 2019 (which was removed as part of the subsampling in Section 3), we still obtain similar ocean and atmospheric conditions in the subsequent summers, compared to those with the outlier excluded (Fig. S6). Specifically, we still identify an increased SST difference between the subpolar cold SST anomaly and the subtropical warm SST anomaly, with the location of the SST front being shifted northward in the second summer relative to the first summer (Fig. S6a and b). Moreover, we still identify northward deflections of the winds and warm and dry anomalies over Europe (Fig. S6c to h), with the locations closely resembling the regressions with the NAO_S year in 2019 excluded (Fig. 5c to h). Likewise, if we only include the second anomaly in all consecutive anomalies, the results also remain similar and significant (Fig. S7).

Next we examine the sensitivity of the results to the number of years included in the F_W subset. Since we find that the results do not change appreciably when we include or exclude single years, we show how the results are changing when we add or remove years in increments of 5 years. Thus, we show the regressions for $N = 7$ (Fig. S8), $N = 12$ (Fig. S9), $N = 17$ (Fig. 6 in the main manuscript), $N = 22$ (Fig. S10), $N = 27$ (Fig. S11) and $N = 32$ (Fig. S12), with N corresponding to the number of years included. The choice of years follows the same method as before (Section 3), with the objective of maximising the regression slope and the variance (resulting in high correlations). Thus, we rank all years according to the term $(y_i - y) \cdot (x_i - x_0)$ (Section 3.2) and then select the N highest terms.

The regressions for the case, where no further subsampling is applied after excluding the F_E subset and the two outliers (corresponding to $N = 33$, not shown), do not change appreciably compared to the regressions where $N = 32$. Likewise, if we exclude the only remaining consecutive year from the case where $N = 7$ (not shown), the results do not change appreciably compared to the $N = 7$ case. Overall, we find: The lower the number of years, the higher is the amplitude of the correlations and regressions. The higher correlations compensate for the reduced number of degrees of freedom in the significance estimates. In addition to the higher amplitudes of the correlations and regressions, the location of the maximum warm and dry anomalies can shift in accordance of the location of the associated summer SST anomalies. However, in all cases we identify an increased SST difference between the subpolar cold anomaly and the warm North Atlantic Current, a northward deflection of the lower tropospheric winds west of the European coastline, and warm and dry atmospheric anomalies over parts of western Europe or the eastern North Atlantic.

Lastly, we tested if the results obtained with the ΔSST index (Fig. 7) remain significant if we lowpass filter the atmospheric anomalies in summer and assume a smaller number of degrees of freedom. In the lowpass filtering, we only consider the summer months (July and August). The filter does not include any other months. Thus, we lowpass filter the SST, winds at 700 hPa, the 2-m air temperature and precipitation minus evaporation variability with a 3-summer hanning filter. After the filtering, the resulting autocorrelations of European summer weather are still smaller than the one for the ΔSST index, implying that the number of degrees of freedom based on the ΔSST index underestimates (but not overestimates) the actual number of degrees of freedom. Using the autocorrelations of the ΔSST index, we estimate $N^* = \frac{N\Delta t}{2T_e} - 2$ degrees of freedom, where N here is the number of data points, Δt is the time interval between them, and T_e is the e-folding timescale of the autocorrelations (Leith, 1973), which is 2 years for the ΔSST index (Fig. 8a). While the regressions remain significant, their amplitude weakens (Fig. S13), indicating that the interannual variability, which has been filtered out, must have contributed to the increased relationship in the regressions obtained from the unfiltered time series (Fig. 7).

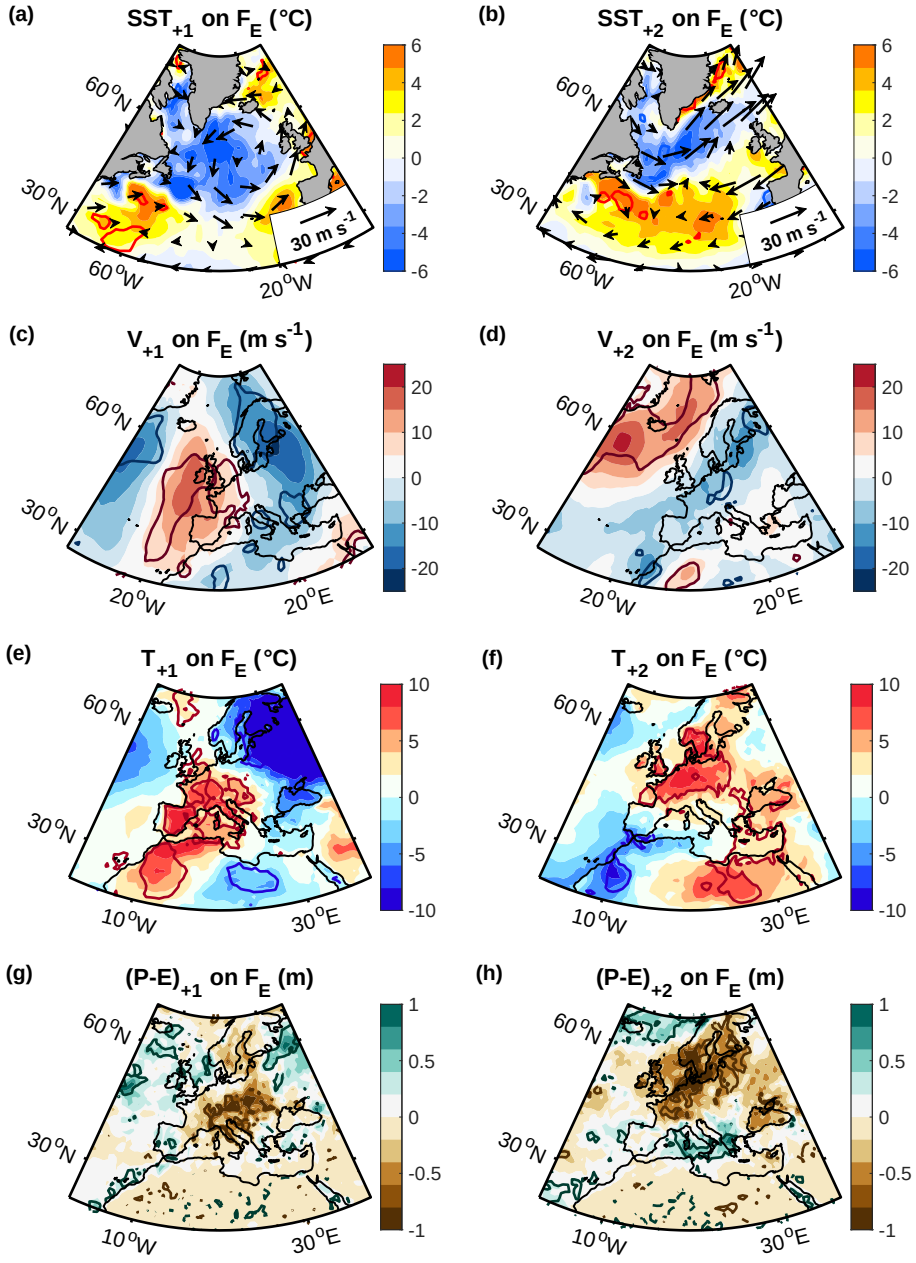

Figure S6. As in Figure 5 of the main manuscript, but with the NAO_S index in 2019 included in the F_E subset.

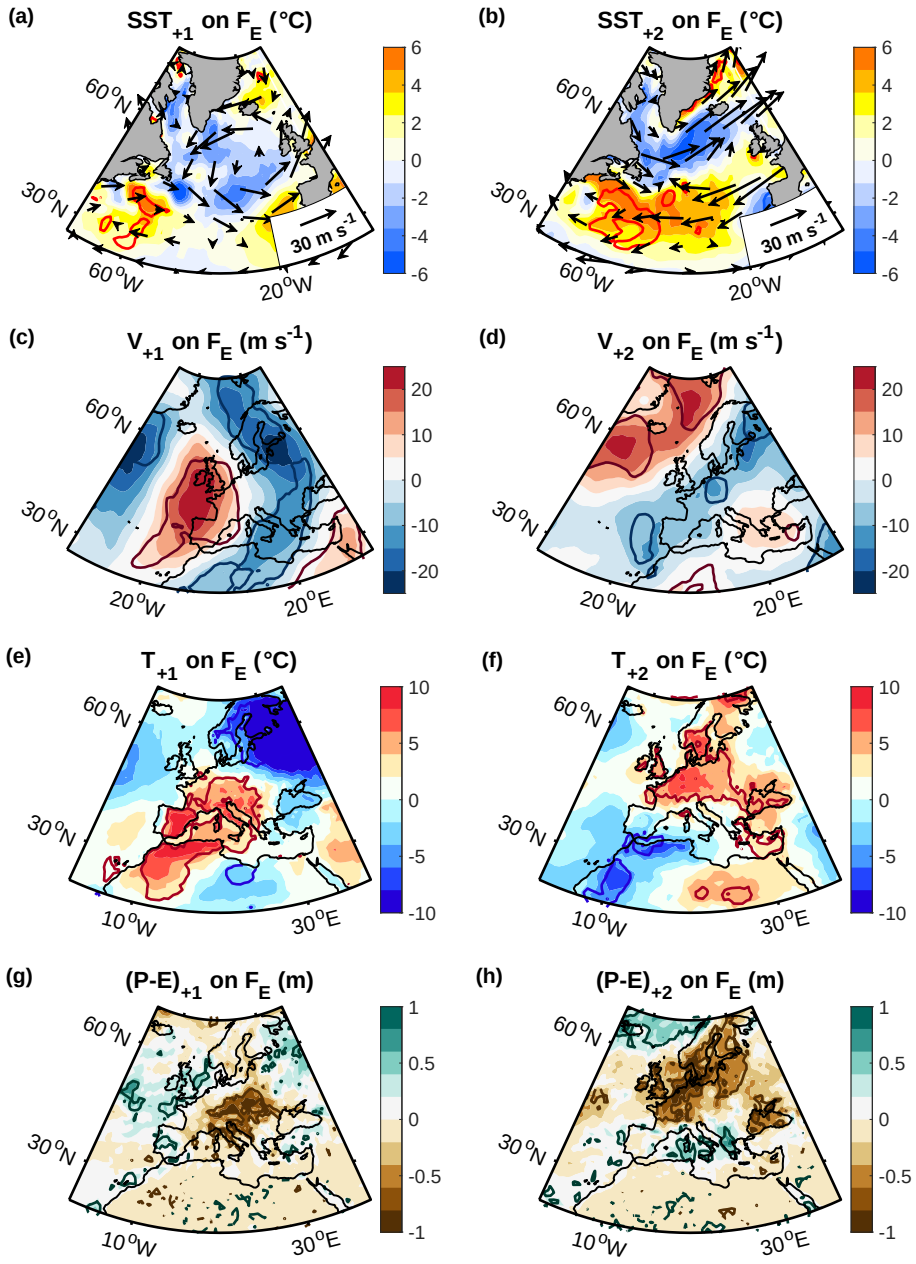

Figure S7. As in Figure 5 of the main manuscript, but excluding all consecutive years. Specifically, we only included the second year in all consecutive years to avoid overlapping anomalies. Thus, the regression is based on the NAO_S years 1980, 1993, 2009, 2012 and 2016.

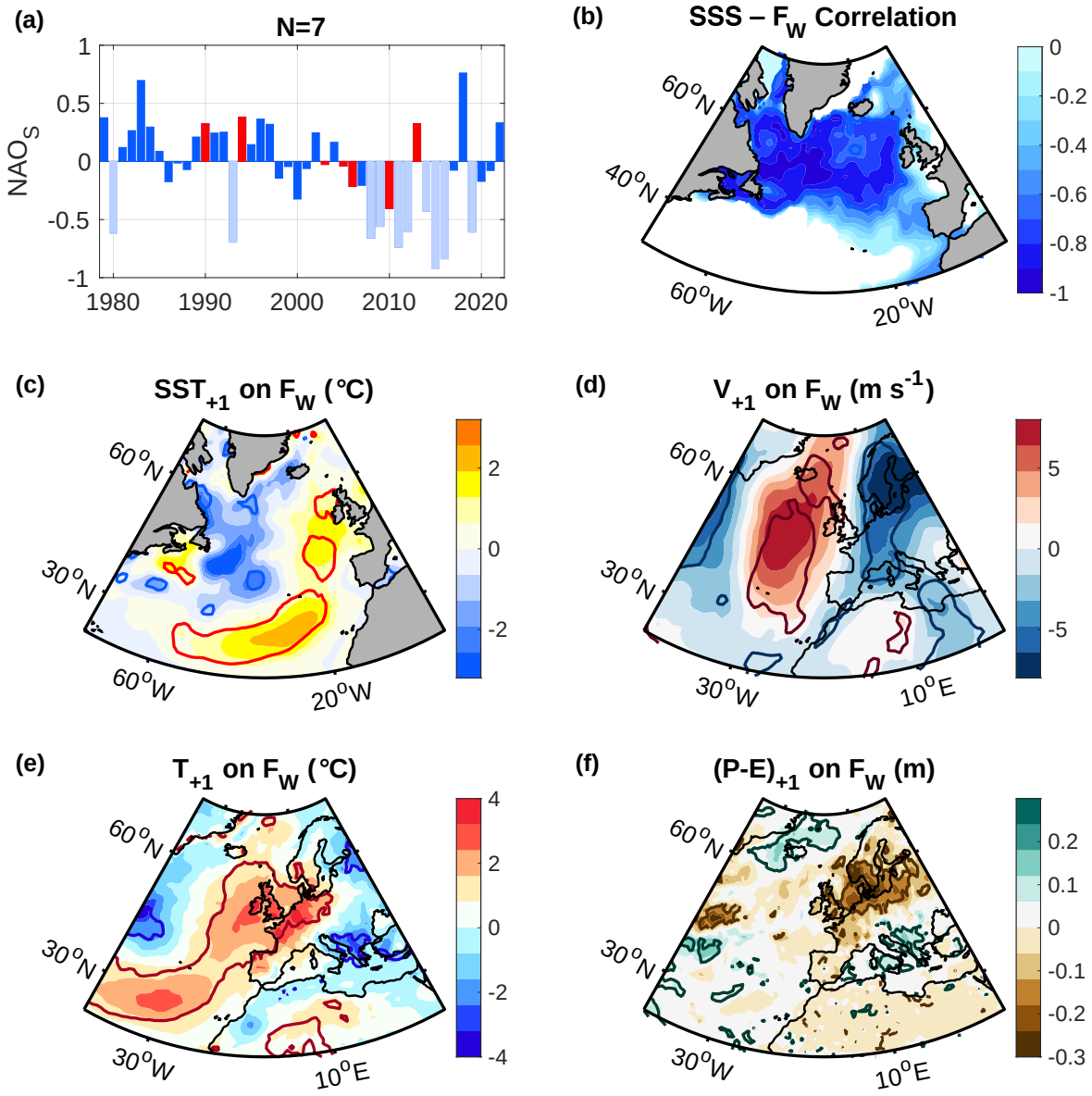

Figure S8. (a) NAO$_S$ index with the years included in the F$_W$ subset shown in red. Years excluded prior to the subsampling (including the 8 F$_E$ years and the two outliers) are shown as faint blue bars. (b) Correlation between the F$_W$ subset (the red NAO$_S$ years in panel a) and the associated SSS anomaly in the subsequent winter (January to March), estimated from the surface mass balance by assuming density compensation. (c-f) Regressions as in Figure 6 of the manuscript but including only 7 years in the F$_W$ subset (shown in panel a). The thick contours encompass regions that are significant at the 95% confidence level.

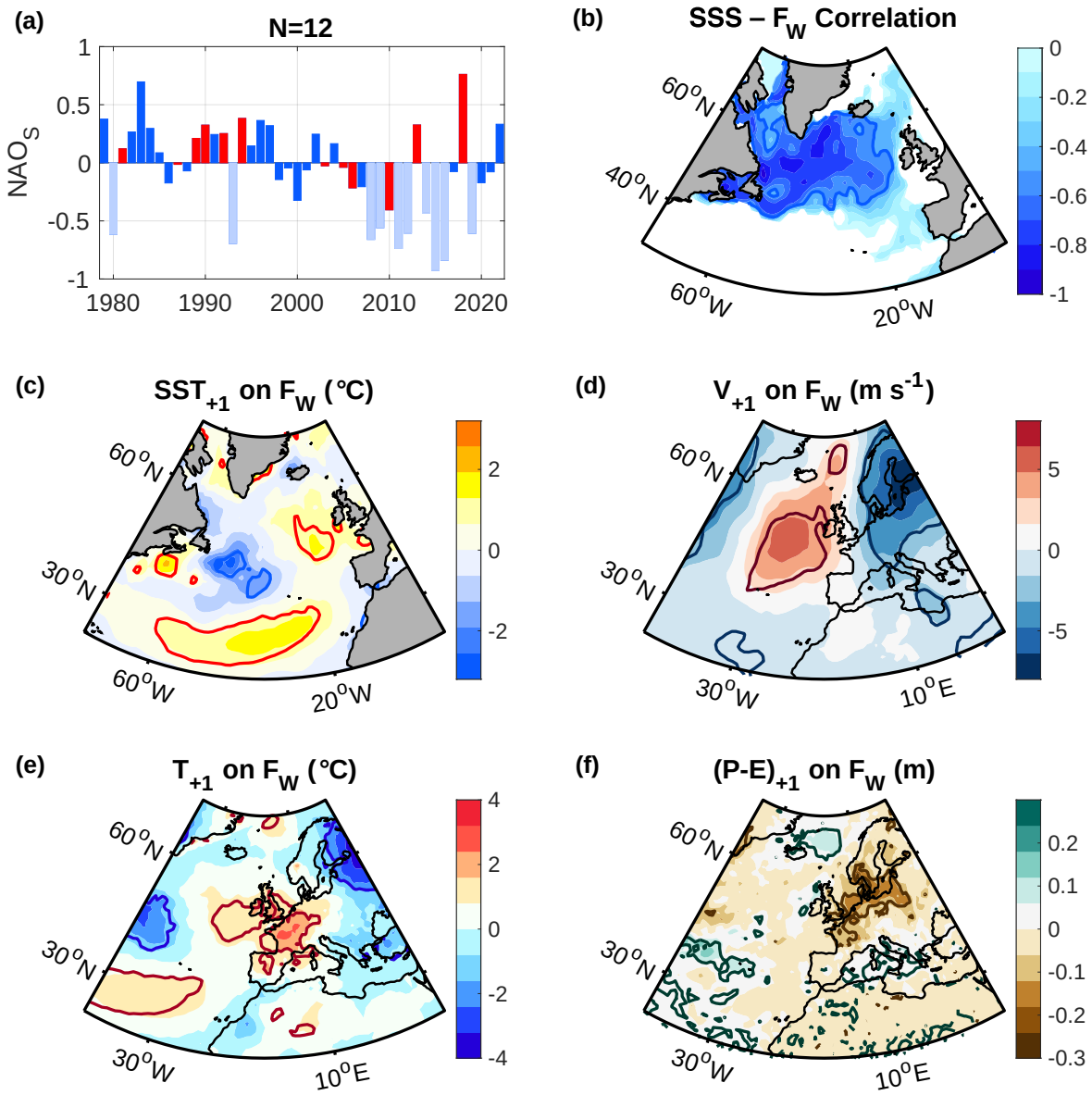

Figure S9. As in Figure S8 but for $N = 12$ years.

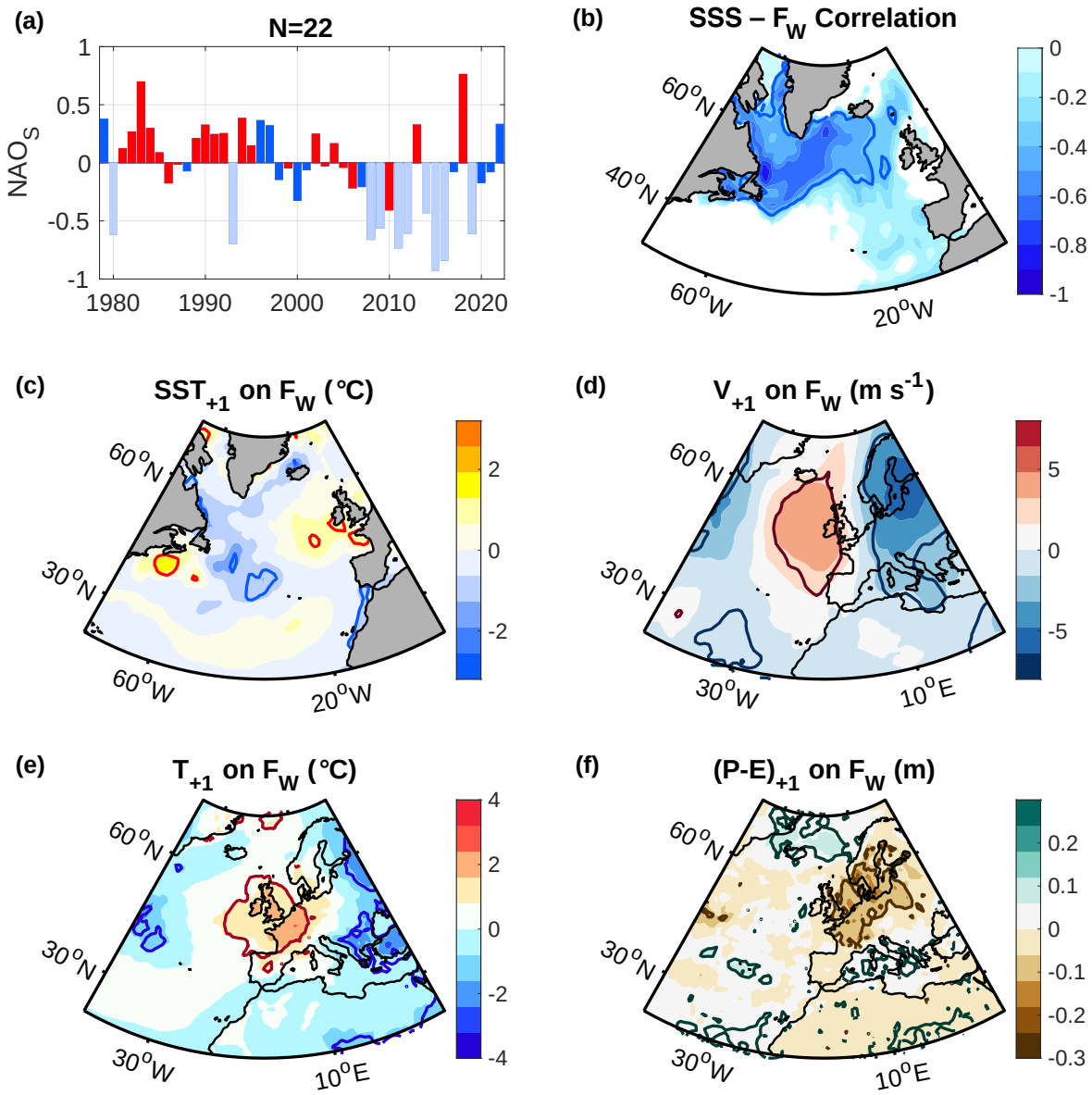

Figure S10. As in Figure S8 but for $N = 22$ years.

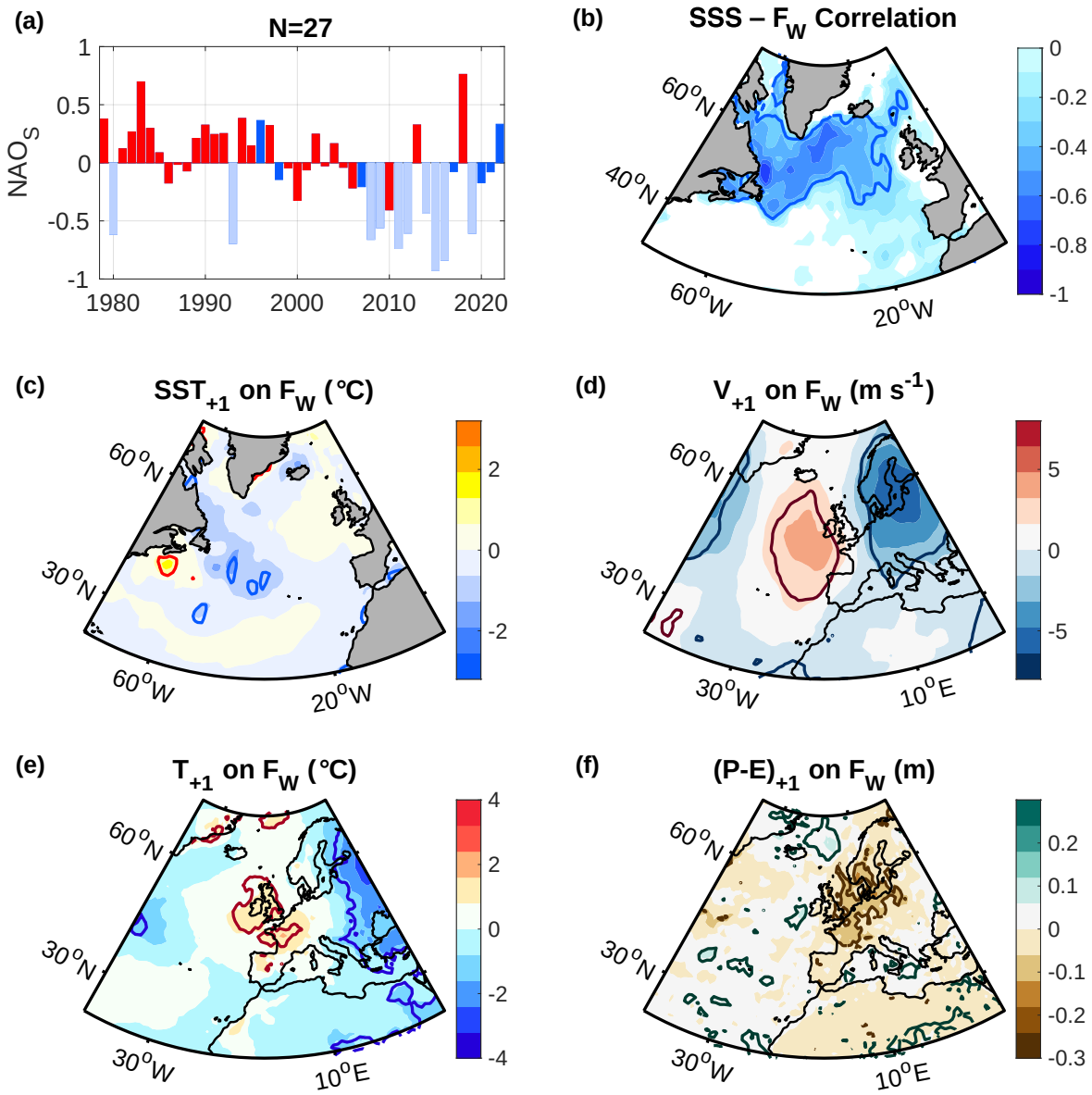

Figure S11. As in Figure S8 but for $N = 27$ years.

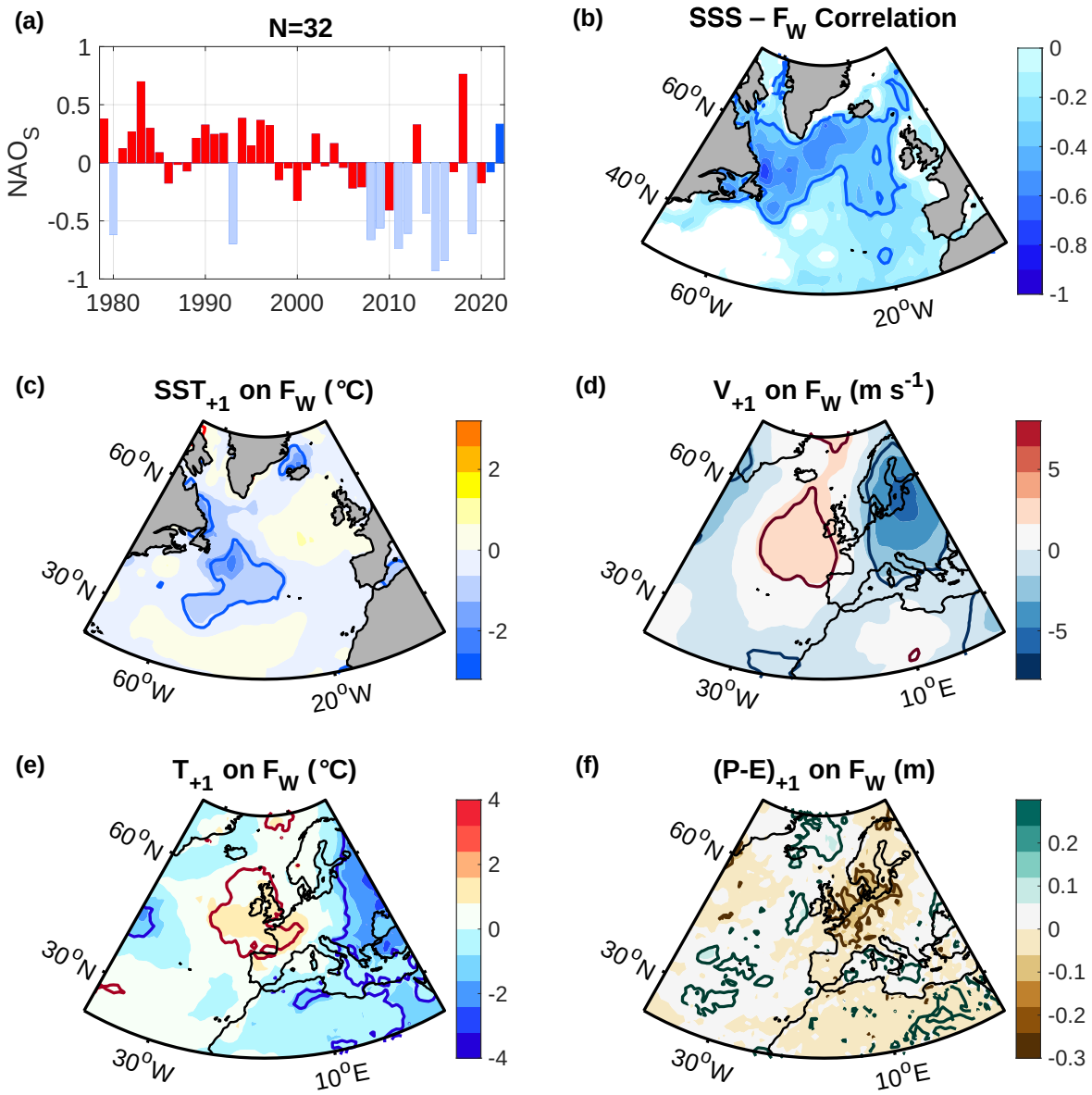

Figure S12. As in Figure S8 but for $N = 32$ years.

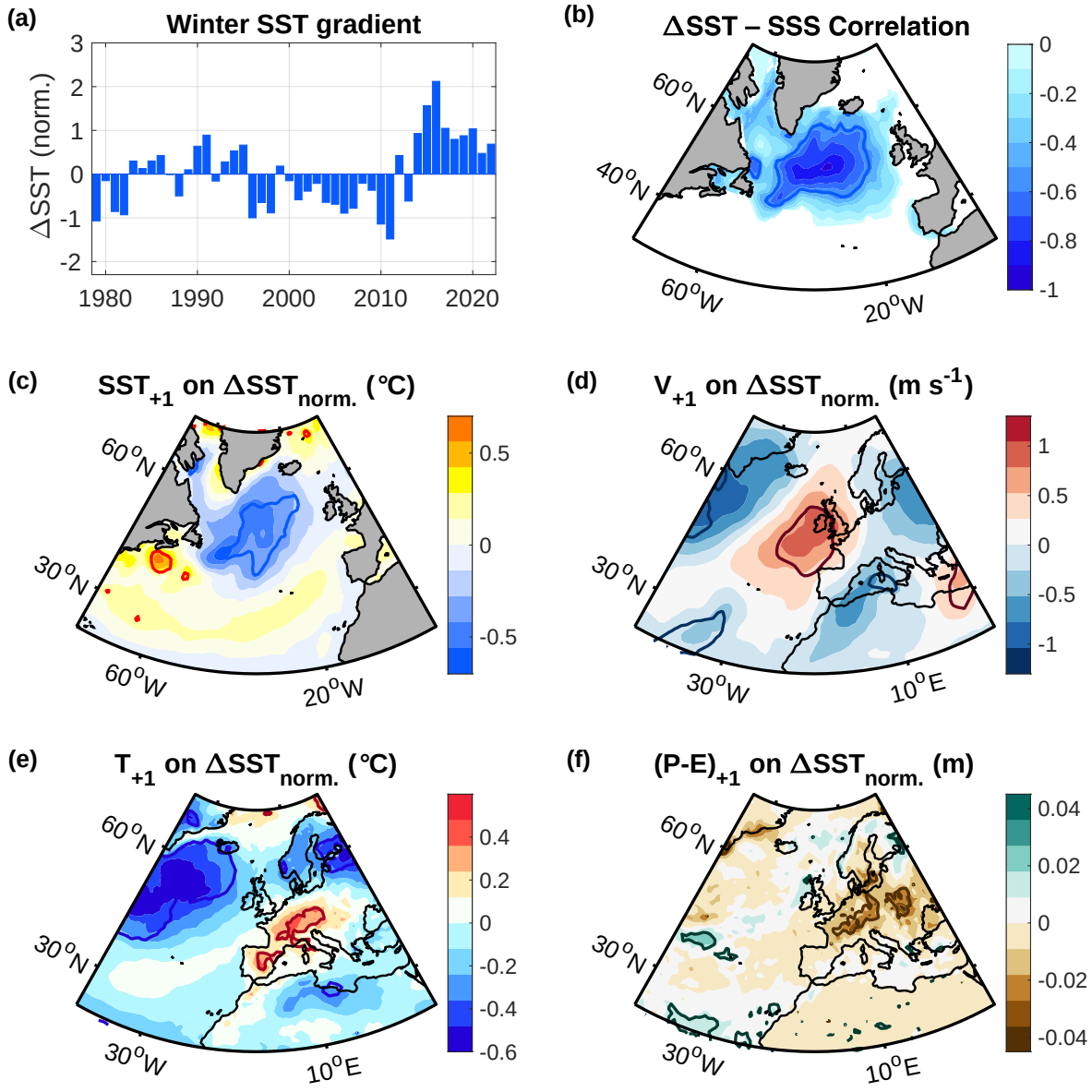

Figure S13. As in Figure 7 of the manuscript, but after lowpass filtering the SST in summer (July and August), the 700 hPa winds in summer, and the 2-m air temperature and precipitation minus evaporation anomalies in summer, with a 3-summer hanning filter. The total number of degrees of freedom in the significance tests in all panels was estimated with $\frac{N\Delta t}{2T_e} - 2 = 9$, where N is the number of years (which is 44), Δt is one year, and T_e is the lag where the correlation drops to the e-folding value ($\sim$0.37), corresponding to $\sim$2 years for the ΔSST index.

References

Bao, S., Wang, H., Zhang, R., Yan, H., and Chen, J.: Comparison of satellite-derived sea surface salinity products from SMOS, Aquarius, and SMAP, Journal of Geophysical Research: Oceans, 124, 1932–1944, 2019.

Gill, A. E.: Atmosphere-ocean dynamics, vol. 30, Academic press, ISBN 978-0122835223, 1982.

Holte, J., Talley, L. D., Gilson, J., and Roemmich, D.: An Argo mixed layer climatology and database, Geophysical Research Letters, 44, 5618–5626, 2017.

Leith, C.: The standard error of time-average estimates of climatic means, Journal of Applied Meteorology (1962-1982), pp. 1066–1069, 1973.

McDougall, T., Feistel, R., Millero, F., Jackett, D., Wright, D., King, B., Marion, G., Chen, C., Spitzer, P., and Seitz, S.: The international thermodynamic equation of seawater 2010 (TEOS-10): Calculation and use of thermodynamic properties, Global ship-based repeat hydrography manual, IOCCP report no, 14, 2009.

Piron, A., Thierry, V., Mercier, H., and Caniaux, G.: Gyre-scale deep convection in the subpolar North Atlantic Ocean during winter 2014–2015, Geophysical Research Letters, 44, 1439–1447, 2017.

Timlin, M. S., Alexander, M. A., and Deser, C.: On the reemergence of North Atlantic SST anomalies, Journal of climate, 15, 2707–2712, 2002.

Xie, J., Raj, R. P., Bertino, L., Samuelsen, A., and Wakamatsu, T.: Evaluation of Arctic Ocean surface salinities from the Soil Moisture and Ocean Salinity (SMOS) mission against a regional reanalysis and in situ data, Ocean Science, 15, 1191–1206, 2019.

Yashayaev, I. and Loder, J. W.: Further intensification of deep convection in the Labrador Sea in 2016, Geophysical Research Letters, 44, 1429–1438, 2017.